Received: 29 July 2024 | Revised: 4 November 2024 | Accepted: 27 December 2024 | Published online: 21 January 2025

RESEARCH ARTICLE

Journal of Optics and Photonics Research
2025, Vol. 00(00) 1–8
DOI: 10.47852/bonviewJOPR52023980

BON VIEW PUBLISHING

Optical Transmission Enhancement of MoS_2 Nanosheets Doped with Magnetic Materials Ni, Mn, and Cr

Sondes Kaddour[1], Randa Zaimia[1], Nouha Mastour[1], Said Ridene[1,*] and Noureddine Raouafi[2]

[1]*Faculty of Sciences of Tunis, University of Tunis El Manar, Tunisia*

[2]*Chemistry Department, University of Tunis El Manar, Tunisia*

Abstract: In this work, we report both theoretical and experimental study of the influence of some materials with magnetic aspects such as Ni, Mn, or Cr in MoS_2 photonic crystal structures. A functional density method technique has been introduced. Indeed, the results indicated that the transmission spectrum is considerably affected by the impact of doping from a photo shape and amplitude. Furthermore, appropriate doping has been shown to change the peak transmission shape of the MoS_2 photonic crystal by splitting as an example. In fact, the transmission spectrum remains less identical with Ni and Mn doping and exhibits a doubling peak with Cr attributed to the first and second waveguide propagation modes. The obtained results can give a new degree of freedom in device application of MoS_2 nanosheets such as photonic sensors, filter, and reflector. Finally, we can predict that the MoS_2 photonic crystal doped with magnetic materials could be used in applications involving plasmonic Fano-resonances.

Keywords: doped MoS_2 photonic structures, 2D materials, magnetic doping materials, transmission spectrum, Fano-resonances

1. Introduction

Impressive progress on the doping of photonic structures based on (Graphene, MoS_2, $MoSe_2$, WS_2, WSe_2, etc.,) has recently been reported [1, 2]. Most of the experimental and theoretical studies for photonic structures have been reported to be one- and two-dimensional photonic crystal based on III–V, II–VI, VI–VI semiconductors, due to their wide applications [3–5]. Moreover, graphene and equivalent 2D materials based on MoS_2 can be also used in the dispositive of photonic structures due to their remarkable refractive index which is beneficial for confinement and transmission of light [6–10]. Despite MoS_2 nanostructures having a direct band gap, they display lower quantum yield and poor photoluminescence (PL) intensity at room temperature [11, 12]. The origin of the poor PL has been attributed to the little absorption, which is smaller than 10%, while the lower quantum yield is attributed to nonradiative recombination and to bi-excitonic recombination [13]. Therefore, MoS_2 nanosheets will be limited for many applications and it is necessary to introduce light doping to resolve these problems of optical absorption. The doping of MoS_2 has been considered one of the best techniques to enhance several physical properties of MoS_2 such as the transmittance. In this paper, we study the incorporation of MoS_2 nanosheets for the photonic guide structure taking into account the influence of doping by materials with magnetic effects materials such as Ni, Mn, and Cr [14–19]. In particular, we discuss the effect on the amplitude of the transmission spectrum and the origin of the peaks which can be attributed to the polarization effect or to the Fano-resonance phenomenon [20]. Furthermore, the Fano-resonances can be manifested in classical and quantum systems thanks to the interference between two paths [21]. Compared to a conventional resonance, characterized by a Lorentzian spectral response, the Fano-resonance is a typical irregular and loud spectral results suggested to enable photonic switches and sensors with good characteristics. Indeed, several experimental demonstrations of the appearance of Fano-resonances have been made in plasmonic and photonic crystal structures [22, 23]. The numerical step is based on both PWE and functional density method (*FDTD)* approaches which have been proved competent in the investigations of various kinds of 3D-, 2D-, and 1D-photonic crystal structures [24]. In the experimental phase, we applied hydrothermal method in order to synthesize the MoS_2 nanosheets.

2. XRD, Raman, and PL Spectra of MoS_2 Nanosheets Doped with Ni, Mn, and Cr

In the elaboration of MoS_2 nanosheets, we apply the hydrothermal technique to prepare pure and X-doped MoS_2 [25] (X: Ni, Mn, or Cr). The MoS_2 can be obtained from the consecutive precursors such as the ammonium heptamolybdate ($(NH_4)_6Mo_7O_{24}$) and the thiocarbamide (CH_4N_2S):

$$CSN_2H_4 + 2H_2O \rightarrow 2NH_3 + H_2S \quad \text{(I)}$$

$$(NH_4)_6Mo_7O_{24} \rightarrow 6NH_3 + 7MoO_3 + 3H_2O \quad \text{(II)}$$

*Corresponding author: Said Ridene, Faculty of Sciences of Tunis, University of Tunis El Manar, Tunisia. Email: said.ridene@fst.rnu.tn

$$MoO_3 + 3H_2S + H_2O \rightarrow MoO_2 + SO_4^{2-} + 2H^+ \quad \text{(III)}$$

$$MoO_2 + 2H_2S \rightarrow MoS_2 + 2H_2O \quad \text{(IV)}$$

$$NiCl_2 \rightarrow Ni^{2+} + 2Cl^- \quad \text{(V)}$$

Similarly, to the previous step, Ni-nitrate is combined with the solution of MoS_2 for the synthesis of Ni-MoS_2 for different concentration. We have used XRD, transmission electron microscopy (TEM), Raman, and PL spectroscopies. Figure 1(a), (b), (c), and (d) shows the XRD diagrams patterns, the TEM images, the Raman spectra, and the PL spectra of the MoS_2 nanostructure elaborated for three Ni concentrations (0%, 1%, and 3%).

From Figure 1(a), one can notice that there are strong and sharp diffraction peaks which indicate the good crystallinity of the products of MoS_2. Indeed, these peaks appeared at the angles of 13.51°, 32.52°, 35.84°, and 43.37° designing the (002), (100), (102), and (110) reticular planes, respectively. The unit cell parameters revealed (a = 3.1612 Å, c = 12.2985 Å) have been compared with other previous works [29]. However, they agree with the hexagonal structure and adopt space group symmetry P63/mmc. These data agreed with the corresponding powder diffraction files of MoS_2 database referenced as JCPDS 00-037-1492 [29]. We note that no secondary peaks are detected for Ni-MoS_2 samples, which designated that the MoS_2 are in single phase. Furthermore, one can see that the doped Ni^{3+} ions have not caused change in the structure of the sample. Indeed, the regular diffraction patterns indicate that the single phase is not affected by the small quantities of Ni. Moreover, it is important to note that the optical cavities are particularly useful for controlling the light emission and absorption properties of cavities based on two-dimensional materials because they can interact with photons and use surrounding electromagnetic fields [25–28]. This is evidenced by the PL spectrum of 2D-MoS_2 as shown in Figure 1(d). Therefore, the PL spectra suggest some emission substantial peaks at 340, 495, 532, and 673 nm attributed to the excitonic transitions. Then, two-dimensional MoS_2 presents strong PL intensity, large refractive index, and high exciton binding energy; thus, MoS_2 nanosheets can form a very good candidate for the 2D-photonic crystal dives. Figure 1(c) shows the Raman spectra of the three

Figure 1

(a) XRD patterns of Ni-MoS_2 nanostructures for 0%, 1%, and 3% Ni concentration, (b) TEM de 2D−MoS_2, (c) Raman intensity of MoS_2 nanosheets determined with 633 nm wavelength excitation, and (d) PL-spectra of MoS_2 nanosheets for 0%, 1%, and 3% Ni concentrations

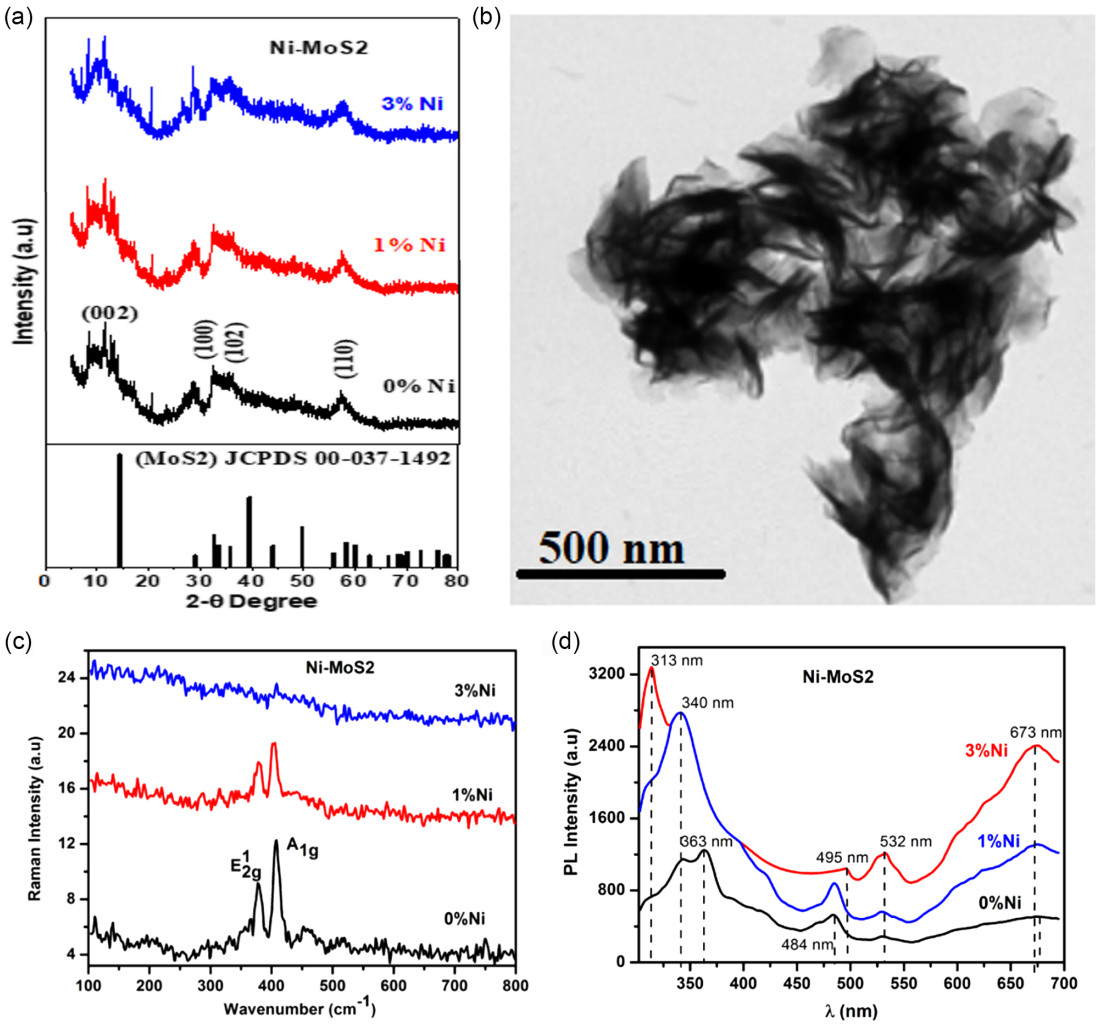

Figure 2
Raman spectra of doped MoS_2: (a) for Mn-MoS_2 and (b) for Cr-MoS_2

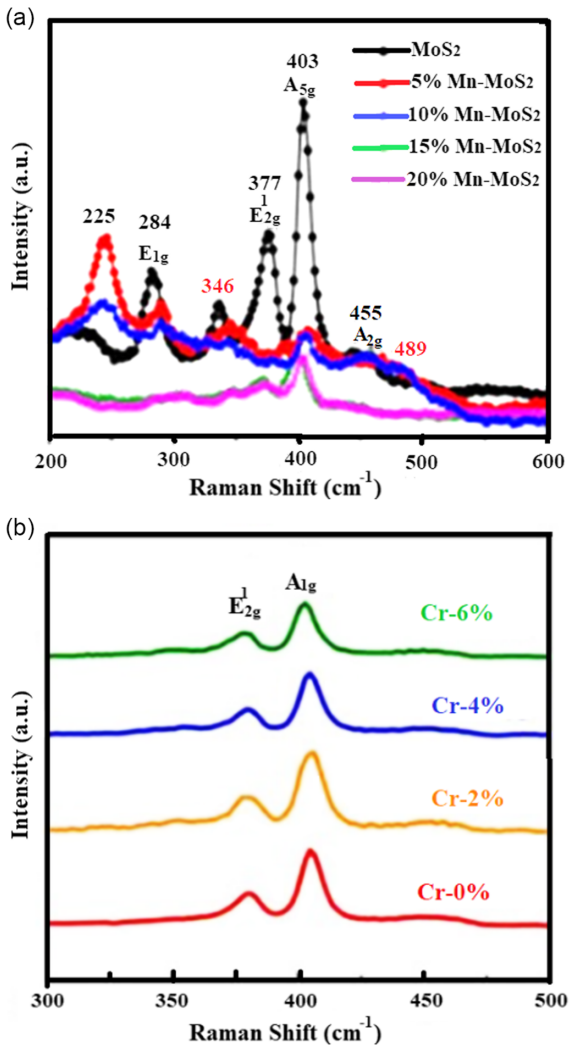

samples (0%Ni, 1%Ni, and 3%Ni) of MoS_2. These spectra are determined at room temperature with T6400 series II spectrometer Raman using an excited laser source between 100 and 800 cm^{-1}. The realization of the basic phase of 0%Ni-MoS_2 has been notified by their Raman lines $E_{2g}{}^1$ and A_{1g} at 370 and 410 cm^{-1}, respectively, and it is observed to be in respectable accord with the experimental analyses [28–31]. One can notice that when Ni-composition is increased from 1% to 3%, the specific peak intensity decreases significantly and shift faintly for the shorter wavenumber. Figure 2 shows the Raman spectra of Mn-MoS_2 and Cr-MoS_2 extracted from reference [25, 26], respectively.

The difference between MoS_2 samples doped with Ni and Cr and Mn can be observed in the Raman spectral of Figures 1(c) and 2 [25–32]. The mean difference between these dopant elements essentially resides in the position and the frequency width between the two principal peaks $E_{2g}{}^1$ and A_{1g} vibration modes. Furthermore, it is well known that the number of material layers can be determined from the difference frequency between $E_{2g}{}^1$ and A_{1g} vibration modes [24]. Therefore, the frequency difference between $E_{2g}{}^1$ and A_{1g} is of about 26 cm^{-1}, 24 cm^{-1}, and 23 cm^{-1} for Ni-MoS_2, for Cr-MoS_2, and for Mn-MoS_2, respectively. Thus, these differences between the two vibration

Figure 3
High-resolution transmission electron microscopy (HRTEM)/ transmission electron microscopy (TEM) of 2D-MoS_2 doped with (a) 0% Ni, (b) 5% Ni, (c) 0% Cr, (d) 4% Cr (e) 0% Mn, and (f) 5% Mn

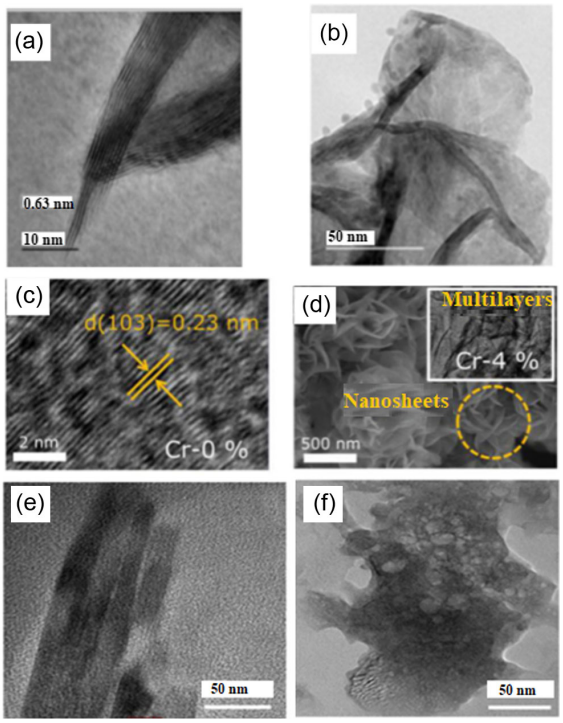

modes indicate the formation of less than ten layers of the doping materials, which can confirm the 2D structure of the MoS_2.

Figure 3 illustrates the morphology and the MoS_2 nanostructure size attained with the TEM extracted from reference [25, 26], respectively. Indeed, flower-like structural design has been detected, and some lateral size of the MoS_2 nanosheets is determined for 0% and 5% of Ni, Cr, and Mn.

The small increase in TEM illustrations in Figure 3(a), (b), (c), (d), (e), and (f) designate the thin morphology and the lamellar structure of MoS_2 0% and 5% of Ni, Cr, and Mn, respectively. However, we will applicate the 2D method of *FDTD* technique for the study of MoS_2 nanosheets in the theoretical step.

3. Theoretical Study and Mathematical Framework

The incorporation of the doped MoS_2 in photonic crystals can cause several interesting and potentially useful effects related to resonant coupling between the confined light and elementary excitations. It is worth noting that by studying the phenomenon of auto-ionization of helium atoms, U. Fano discovered the type of resonance called Fano-resonance [23]. The characteristics of this resonance have an asymmetrical profile; otherwise, an abrupt passage of a minimum of transmission towards maximum transmission will be produced. This phenomenon can be identified in photonic crystals, plasmonic nanoparticles, and electromagnetic metamaterials. It is worth noting that the so-called Purcell effect has been used to increase the spontaneous emission rate of the active gain of 2D material by localized modes of nanostructures [7, 8]. Thus, during the lower coupling regime the exciton in 2D-semiconductors

interacts with the optical cavity modes of the nanostructures [9–12], while in the strong coupling regime, the interaction between 2D materials and nanostructures [10, 13, 20] causes an exchange of energy between the excitons as well as the optical modes which will be introduced and accompanied by a complex spontaneous emission and a doubling of the spectrum known by the Rabi division effect [21, 22]. This condition can generate the excitons-polaritons which allowed the control and manipulation of light [10, 23, 24]. As quasiparticles, excitons-polaritons offer the advantages of the notion of effective mass m*, the fast propagation speed, the long-distance space-time coherence while they have a strong interaction which can improve nonlinear properties [25]. In this section, we used a *FDTD* simulation in our model for TE (transverse electric) ($\boldsymbol{E_z}$, $\boldsymbol{H_x}$, $\boldsymbol{H_y}$) and transverse magnetic ($\boldsymbol{H_z}$, $\boldsymbol{E_x}$, $\boldsymbol{E_y}$) modes. This method solves Maxwell's equations by discretizing both space and time. In the absence of free charges, Maxwell's equations are written in the following differential form:

$$\overrightarrow{rot}\,\vec{E} = -\frac{\partial \vec{B}}{\partial t} \tag{1}$$

$$\overrightarrow{rot}\,\vec{H} = \frac{\partial \vec{D}}{\partial t} \tag{2}$$

$$\operatorname{div}\vec{E} = 0 \tag{3}$$

$$\operatorname{div}\vec{H} = 0 \tag{4}$$

where $\vec{B}$ and $\vec{D}$ represent respectively the magnetic induction and the electric displacement of the medium. The projection of Equations (1) and (2) into a Cartesian frame of coordinates x, y, and z gives:

$$\frac{\partial \overrightarrow{H_x}}{\partial t} = \frac{1}{\mu}\left(\frac{\partial \overrightarrow{E_y}}{\partial z} - \frac{\partial \overrightarrow{E_z}}{\partial y}\right) \tag{5}$$

$$\frac{\partial \overrightarrow{H_y}}{\partial t} = \frac{1}{\mu}\left(\frac{\partial \overrightarrow{E_z}}{\partial x} - \frac{\partial \overrightarrow{E_x}}{\partial z}\right) \tag{6}$$

and

$$\frac{\partial \overrightarrow{H_z}}{\partial t} = \frac{1}{\mu}\left(\frac{\partial \overrightarrow{E_x}}{\partial y} - \frac{\partial y}{\partial x}\right) \tag{7}$$

$$\frac{\partial \overrightarrow{E_x}}{\partial t} = \frac{1}{\varepsilon}\left(\frac{\partial \vec{z}}{\partial y} - \frac{\partial \overrightarrow{E_y}}{\partial z}\right) \tag{8}$$

$$\frac{\partial \overrightarrow{E_x}}{\partial t} = \frac{1}{\varepsilon}\left(\frac{\partial \overrightarrow{E_x}}{\partial z} - \frac{\partial \overrightarrow{E_z}}{\partial x}\right) \tag{9}$$

$$\frac{\partial \overrightarrow{E_x}}{\partial t} = \frac{1}{\varepsilon}\left(\frac{\partial \overrightarrow{E_y}}{\partial x} - \frac{\partial \overrightarrow{E_x}}{\partial y}\right) \tag{10}$$

FDTD is based on Yee's [28] algorithm whose space and time coordinates are written as a function of integer indices i, j, k and n: $x = i\Delta x$, $y = j\Delta y$, $k = k\Delta z$, and $t = n\Delta t$ with Δx, Δy, and Δz are spatial steps respectively along x, y, and z and Δt the time period. Thus, the

Figure 4
Yee scheme 3-dimensional spatial discretization

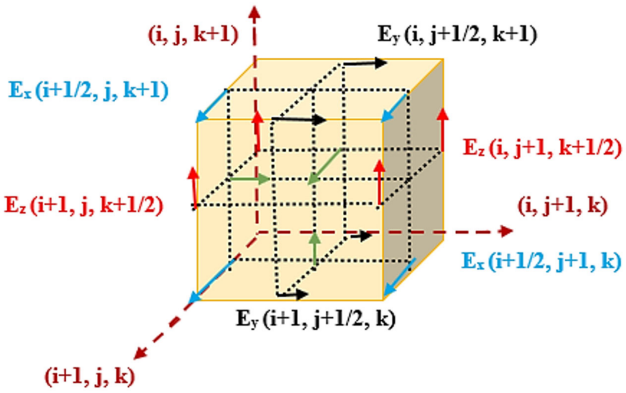

resolution of the previous system of equations is based on a discretization scheme (Figure 4 [28]) with centered finite differences where the spatial and temporal derivatives of the components u (xi, yj, zk, t) are approximated from their Taylor expansion at the second order. If u a component of the electromagnetic field, it can be written as follows:

$$u(xi, yj, zk, t) = u(i\Delta x, j\Delta y, k\Delta z, n\Delta t) = u^{n}{}_{i,j,k} \tag{11}$$

The spatial derivative along x of u is then given by:

$$\frac{\partial u^{n}_{i,\ j,\ k}}{\partial x} = \frac{\left(u^{n}_{i+\frac{1}{2},\ j,\ k}\right) - \left(u^{n}_{i-\frac{1}{2},\ j,\ k}\right)}{\Delta x} + \circ\left([\Delta x]^2\right) \tag{12}$$

The same goes for the time derivative:

$$\frac{\partial u^{n}_{i,\ j,\ k}}{\partial t} = \frac{\left(u^{n+1/2}_{i,\ j,\ k}\right) - \left(u^{n-1/2}_{i,\ j,\ k}\right)}{\Delta t} + \circ\left([\Delta t]^2\right) \tag{13}$$

The electric components are determined at $n\Delta t$ times, and the magnetic components are shifted by half a time step and therefore evaluated at $(n + 1/2)\Delta t$ times.

The expansion of the equations from (5) to (10) according to the Yee [28] scheme gives:

$$H_x^{n+1/2}(i,j,k) = H_x^{n-1/2}(i,j,k) + \frac{\Delta t}{\mu}\left[\frac{E_y^n(i,\ j,\ k+1) - E_y^n(i,\ j,\ k)}{\Delta z} - \frac{E_z^n(i,\ j+1,\ k) - E_z^n(i,\ j,\ k)}{\Delta y}\right] \tag{14}$$

$$H_y^{n+1/2}(i,j,k) = H_y^{n-1/2}(i,j,k) + \frac{\Delta t}{\mu}\left[\frac{E_z^n(i+1,\ j,\ k) - E_z^n(i,\ j,\ k)}{\Delta x} - \frac{E_x^n(i,\ j,\ k+1) - E_x^n(i,\ j,\ k)}{\Delta z}\right] \tag{15}$$

$$H_z^{n+1/2}(i,j,k) = H_z^{n-1/2}(i,j,k) + \frac{\Delta t}{\mu}\left[\frac{E_x^n(i,\ j+1,\ k) - E_x^n(i,\ j,\ k)}{\Delta y} - \frac{E_y^n(i+1,\ j,\ k) - E_y^n(i,\ j,\ k)}{\Delta x}\right] \tag{16}$$

$$E_x^{n+1}(i,j,k) = E_x^n(i,j,k) + \frac{\Delta t}{\varepsilon}\left[\frac{H_z^{n+1/2}(i,\ j,\ k) - H_z^{n+\frac{1}{2}}(i,\ j-1,\ k)}{\Delta y} - \frac{H_y^{n+1/2}i,\ j,\ k) - H_y^{n+\frac{1}{2}}(i,\ j,\ k-1)}{\Delta z}\right] \quad (17)$$

$$E_y^{n+1}(i,j,k) = E_y^n(i,j,k) + \frac{\Delta t}{\varepsilon}\left[\frac{H_x^{n+1/2}(i,\ j,\ k) - H_x^{n+\frac{1}{2}}(i,\ j,\ k-1)}{\Delta z} - \frac{H_z^{n+1/2}(i,\ j,\ k) - H_z^{n+\frac{1}{2}}(i-1,\ j,\ k)}{\Delta x}\right] \quad (18)$$

$$E_z^{n+1}(i,j,k) = E_z^n(i,j,k) + \frac{\Delta t}{\varepsilon}\left[\frac{H_y^{n+1/2}(i,\ j,\ k) - H_y^{n+\frac{1}{2}}(i-1,\ j,\ k)}{\Delta x} - \frac{H_x^{n+1/2}(i,\ j,\ k) - H_x^{n+\frac{1}{2}}(i,\ j-1,\ k)}{\Delta y}\right] \quad (19)$$

These equations highlight the six components of the electric and magnetic field in the *FDTD* grid as well as the different temporal sampling instants. In three dimensions the CFL criterion is known as (Courant Friedrichs Lewy), and it has the following expression:

$$\Delta t \leq \frac{1}{v_{\max}\sqrt{\frac{1}{\Delta x^2}+\frac{1}{\Delta y^2}+\frac{1}{\Delta z^2}}} \quad (20)$$

v_{max} is the maximum speed of propagation in the medium considered; in general, it is the speed of light in a vacuum. Yee's [28] scheme is characterized by the *CFL* which is a stability criterion to prevent the fields from diverging numerically and having non-physical values. This condition is linked to the time step Δt but also to the space steps

Figure 5
Fano-resonance model, $\eta 1$ and $\eta 2$ represent the fraction of radiation, rD and tD indicate the non-resonant reflection and transmission amplitudes, ηabs signifies the absorption probability correlated with the specified mode

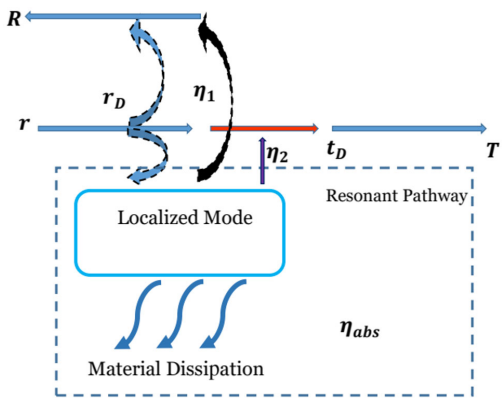

Δx, Δy, Δz, and it represents the boundary condition. Moreover, the Fano-resonance process has been schematically visualized in Figure 5.

Note that the Fano effect, or Fano-resonance, generally refers to the quantum interference between two physical phenomena in the material, where one has a discrete energy spectrum and the other a continuous spectrum [20]. It is highlighted in various spectroscopy experiments such as Raman spectroscopy and absorption spectroscopy by a characteristic asymmetry of the spectral lines. This effect is particularly important for the description of the transport properties and optical spectra of semiconductors.

The expression of the transmission is given by:

$$T(\delta) = |t_D|^2 + 4\frac{\eta_1\eta_2}{1+\delta^2} + 4\frac{|t_D|\sqrt{\eta_1\eta_2}}{1+\delta^2}(\delta\sin\Delta + \delta\cos\Delta) \quad (21)$$

The first term represents the non-resonant contributions, the second term represents also the resonant one, and the final term relates to the interference between them. Δ is the parameter of the phase difference is given [27] in terms of $|t_D|$ and η_n.

$$\Delta = p\ cos^{-1}\left(-|t_D|/\beta^{1/2}\right) \quad (22)$$

$\beta = 4\frac{\eta_1\eta_2}{(\eta_1+\eta_2)^2}$ and p = ±1 depending on the chosen mode.

4. Numerical Modeling

We have structured a photonic ridge waveguide based on MoS_2 and the holes of the structure without air holes of radii $r = 0.36a$ (has the structure parameter, $2r = a$). The normalized frequency of confinement of the electric field is $W = 0.6a/\lambda$. The index taken from the air holes as well as the MoS_2 is respectively $n_{(air)} = 1$, $n_{(MoS2)} = 3.9$ as shown in Figure 6.

In practice, the *FDTD* method will be used to resolve Maxwell equations for several index shape structure. However, the boundary situations and several forms of concerned sources played an important role in numerical step. Thus, we have used the Yee's [28] algorithm with a Gaussian behavior source at times steps attach 17400s, $0.6a/\lambda$ frequency, and 0.003 pulse width, respectively.

4.1. Effect of Ni and Mn on the waveguide ridge structure

Figure 7(a) and (b) illustrates the transmission curve of the ridge waveguide structure of Ni-MoS_2 and Mn-MoS_2 with and without sapphire. It is important to note that the doping atoms change the properties of the waveguide by allowing a decrease in the optical losses and, thus, an increase in the quantum efficiency [3]. We notice that the shape of the MoS_2 transmission curves is consistent

Figure 6
Model of the structure studied based on MoS_2

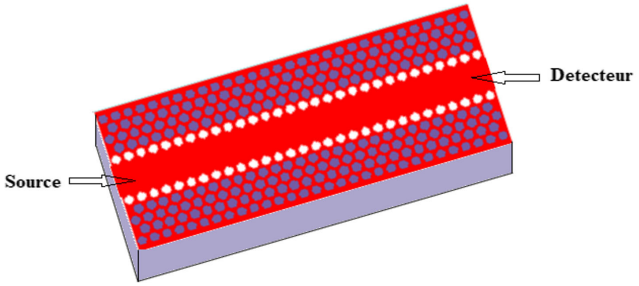

Figure 7
Transmission curve of the ridge waveguide structure calculated with and without sapphire: (a) for Ni-MoS_2 and (b) for Mn-MoS_2

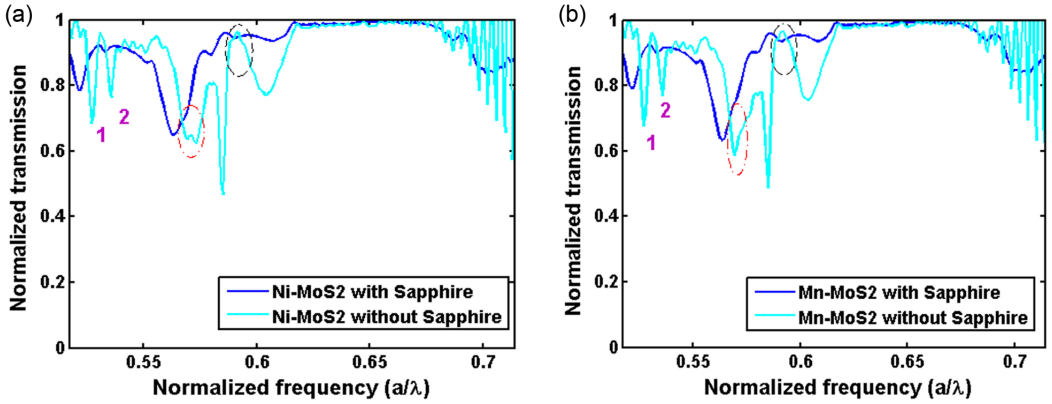

Figure 8
Transmission curve of the ridge waveguide structure calculated with and without sapphire: (a) for Ni-MoS_2 and (b) for Cr-MoS_2

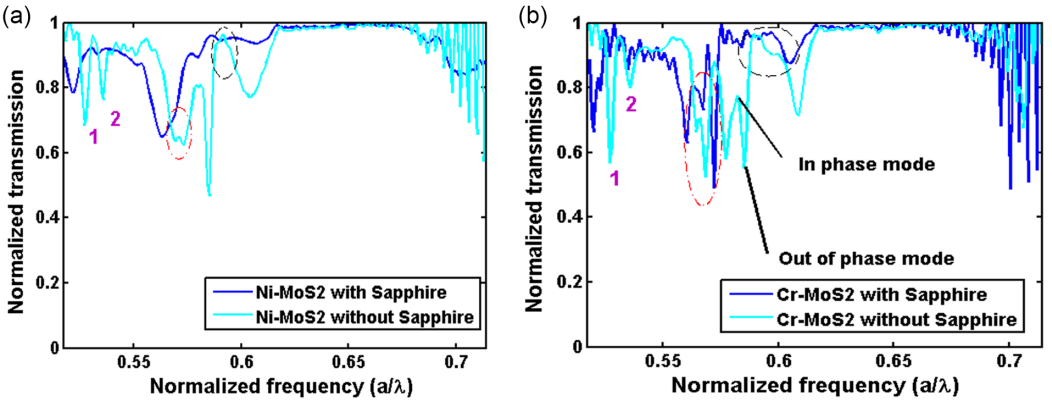

with other studies [33]. However, when the ridge wave structure is based on Sapphire with 2D-MoS_2, the shape of transmission curve in TE mode changes considerably. Further, the doping with Ni can highlight the Fano-resonance, which it has been observed near the *A* and *B* excitons peaks in the resonance phase (light blue) of the excitonic transition as shown in the transmission spectra of Ni-MoS_2 [31].

Moreover, when we compare the results given by Ni-MoS_2 and Mn-MoS_2 structures, one can notice by the circulated zone in red dotted lines the magnetic effect intervenes in the shape of the peak, for Ni-MoS_2 (Figure 7(a)). However, we distinguish a Gaussian shaped peak composed with two transmissions amplitudes $T_1 = 0.634$, $T_2 = 0.623$, respectively. For the case of Mn-MoS_2 (Figure 7(b)), we find a single peak, and the value of the amplitude of transmission of this peak is of a bout of $T = 0.587$ at the normalized frequency of $W = 0.569$ a/λ. This result is in good agreement with the results in reference [31]. It is important to note that Ni- and Mn-MoS_2 have a similarity in the area of the circle (noted by black line) as well as in the shape of the transmission.

4.2. Effect of the Ni and Cr doping

Figure 8(a) and (b) indicates the transmission curve of the ridge waveguide structure Ni-MoS_2 and Cr-MoS_2 with and without sapphire. By comparing the transmission of Ni- and Cr-MoS_2 for the finest peak, we find that the Mn has an important value of transmission $T = 0.4887$ at the frequency $W = 0.585$ a/λ while for the Ni-MoS_2 the transmission peak value is equal to $T = 0.4671$. We have also calculated at the same temperature the quality factor *Q* by the two approaches for TE mode. *Q* is proportional to *FWHM* since it could be written as $Q = \lambda/\Delta\lambda$ where λ is the resonance wavelength and $\Delta\lambda$ is the *FWHM*. Therefore, the numerical calculation has revealed that the *Q* calculated with the model (a) is equal to 167 and the *Q* given by the model (b) is equal to 177.

The $\delta\lambda = 0.004$ a/λ, and variation can be explained by the exchange from the exciton mode *A* to the exciton mode *B*. The transmission spectrum of Cr-MoS_2 remains close to the results found in reference [30].

4.3. Effect of the Mn and Cr doping

Figure 9(a) and (b) indicates the transmission curve of the ridge waveguide structure Mn-MoS_2 and Cr-MoS_2 with and without sapphire. We notice that the Cr is unlike Ni and Mn, and it has an effect on the increase in the number of transmission peaks. Figure 9(b) shows a doubling of two symmetrical peaks area surrounded by a circle of dotted lines in red. The under peaks are generally named by the even and odd modes [27]. In phase mode aspect, the polarization of the field is ordered in the direction − /+ ; − /+ ; − /+ while in the phase out of phase mode the latter is ordered in the direction −/+ ; +/− ; −/ +. The transmission spectra

Figure 9
Transmission curve of the ridge waveguide structure calculated with and without sapphire: (a) for Mn-MoS_2 and (b) for Cr-MoS_2

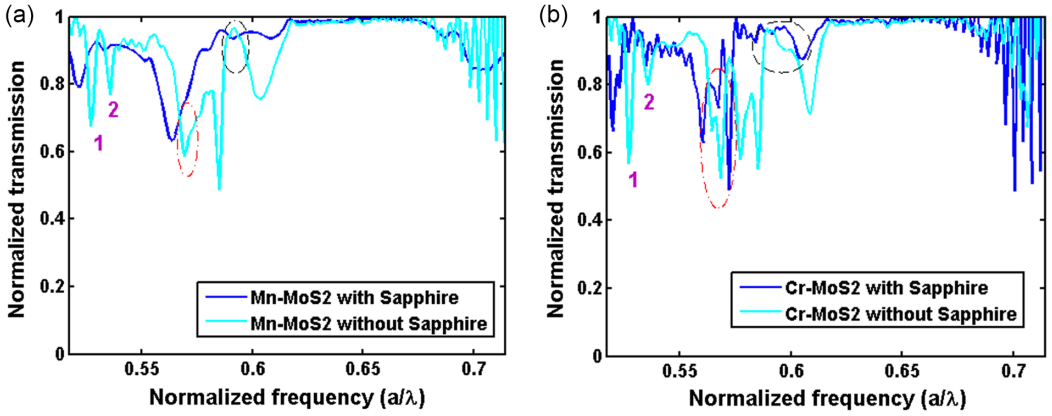

show two Fano-resonance states (named Fano 1 and Fano 2). The Fano-resonance has been observed at the interface of the dopant (Ni or Mn) with MoS_2. The influence of the *Ez* electric field indicates that there is a destructive interaction (Fano2 zone). In addition, the area between the 1st peak Fano1 and the 2nd Fano2 (area circulated in black line) reflects the effect of Cr on MoS_2 at a frequency of the order of $W = 0.594\ a/\lambda$.

On the other hand, the amplitude of the first peak of Cr is of a bout of $T = 0.5693$. This is linked to the morphology of the doped surface, in the result cited in article [30, 31]. The Q factor for Cr-MoS_2 structure is of a bout of $Q = 156$ which is less important than that given by Ni and Mn cases.

5. Conclusion

In this study, we have considered the XRD, Raman, and PL spectra of MoS_2 nanosheets, doped with (0%, 1%, and 3%) of Ni. We have studied within several analysis the influence of (Ni, Mn, and Cr) doping on the variation of transmission of MoS_2 photonic crystal structures. The study indicates that the transmittance behaviors and the quality factor were efficiently modified with Ni, Mn, and Cr doping. The obtained results indicate that the doping with Ni provided a better-quality factor compared to Mn and Cr which can ameliorate the potential of applications of MoS_2 in optoelectronics such as waveguide, reflectors, filters, and sensors.

Ethical Statement

This study does not contain any studies with human or animal subjects performed by any of the authors.

Conflicts of Interest

The authors declare that they have no conflicts of interest to this work.

Data Availability Statement

Data sharing is not applicable to this article as no new data were created or analyzed in this study.

Author Contribution Statement

Sondes Kaddour: Conceptualization, Formal analysis, Writing – original draft. **Randa Zaimia:** Formal analysis, Investigation. **Nouha Mastour:** Validation, Investigation. **Said Ridene:** Methodology, Writing – review & editing, Supervision. **Noureddine Raouafi:** Resources.

References

[1] Ansari, N., Sohrabi, A., Mirbaghestan, K., & Hashemi, M. (2023). Data analysis on the three defect wavelengths of a MoS_2-based defective photonic crystal using machine learning. *Scientific Reports*, *13*, 21699. https://doi.org/10.1038/s41598-023-49013-4

[2] Ma, X., Youngblood, N., Liu, X., Cheng, Y., Cunha, P., Kudtarkar, K., …, & Lan, S. (2021). Engineering photonic environments for two-dimensional materials. *Nanophotonics*, *10*(3), 1031–1058. https://doi.org/10.1515/nanoph-2020-0524

[3] Li, Z., Pang, C., Li, R., & Chen, F. (2020). Low-dimensional materials as saturable absorbers for pulsed waveguide lasers. *Journal of Physics: Photonics*, *2*(3), 031001. https://doi.org/10.1088/2515-7647/ab8a5a

[4] He, Z., Xue, W., Cui, W., Li, C., Li, Z., Pu, L., …, & Li, G. (2020). Tunable Fano resonance and enhanced sensing in a simple Au/TiO_2 hybrid metasurface. *Nanomaterials*, *10*(4), 687. https://doi.org/10.3390/nano10040687

[5] Liu, H., Zheng, L., Ma, P., Zhong, Y., Liu, B., Chen, X., & Liu, H. (2019). Metasurface generated polarization insensitive Fano resonance for high-performance refractive index sensing. *Optics Express*, *27*(9), 13252–13262. https://doi.org/10.1364/OE.27.013252

[6] Barsukova, M., Grisé, F., Zhang, Z., Vaidya, S., Guglielmon, J., Weinstein, M. I., …, & Rechtsman, M. C. (2024). Direct observation of Landau levels in silicon photonic crystals. *Nature Photonics*, *18*, 580–585. https://doi.org/10.1038/s41566-024-01425-y

[7] Takiguchi, M., Takemura, N., Tateno, K., Nozaki, K., Sasaki, S., Sergent, S., …, & Notomi, M. (2020). All-optical InAsP/InP nanowire switches integrated in a Si photonic crystal. *ACS Photonics*, *7*(4), 1016–1021. https://doi.org/10.1021/acsphotonics.9b01705

[8] Sciancalepore, C., Bakir, B. B., Letartre, X., & Viktorovitch, P. (2013). Bridging laser technology to silicon maturity. *SPIE*. https://doi.org/10.1117/2.1201302.004709

[9] Taffelli, A., Dirè, S., Quaranta, A., & Pancheri, L. (2021). MoS_2 based photodetectors: A review. *Sensors*, *21*(8), 2758. https://doi.org/10.3390/s21082758

[10] Jemaï, M., Mastour, N., & Ridene, S. (2024). Linear and nonlinear electric and magneto-optical absorption coefficients and relative refractive index changes in $W_xMo_{1-x}S_2$ monolayer: Role of tungsten contents. *Journal of Nonlinear Optical Physics & Materials*, *33*(2), 2340016. https://doi.org/10.1142/S0218863523400167

[11] Mak, K. F., Lee, C., Hone, J., Shan, J., & Heinz, T. F. (2010). Atomically thin MoS_2: A new direct-gap semiconductor. *Physical Review Letters*, *105*(13), 136805. https://doi.org/10.1103/PhysRevLett.105.136805

[12] Amani, M., Lien, D. H., Kiriya, D., Xiao, J., Azcatl, A., Noh, J., ..., & Javey, A. (2015). Near-unity photoluminescence quantum yield in MoS_2. *Science*, *350*(6264), 1065–1068. https://doi.org/10.1126/science.aad2114

[13] Zhao, J., Gu, Z., & Zhang, Q. (2024). Stacking MoS_2 flower-like microspheres on pomelo peels-derived porous carbon nanosheets for high-efficient X-band electromagnetic wave absorption. *Nano Research*, *17*(3), 1607–1615. https://doi.org/10.1007/s12274-023-6090-3

[14] Saleem, S., Ashiq, M. N., Manzoor, S., Ali, U., Liaqat, R., Algahtani, A., ..., & Zaman, A. (2023). Analysis and characterization of opto-electronic properties of iron oxide (Fe_2O_3) with transition metals (Co, Ni) for the use in the photodetector application. *Journal of Materials Research and Technology*, *25*, 6150–6166. https://doi.org/10.1016/j.jmrt.2023.07.065

[15] Nazir, S., Zhang, J. M., Akhtar, M. N., Abbas, N., Saleem, S., Nauman, M., & Ali, A. (2023). Modification of physicochemical and electrical characteristics of lead sulfide (PbS) nanoparticles (NPs) by manganese (Mn) doping for electronic device and applications. *Journal of Sol-Gel Science and Technology*, *108*(3), 778–790. https://doi.org/10.1007/s10971-023-06176-w

[16] Wei, R., Liu, G., Gao, X., He, J., Zhao, J., Chen, Y., & Zhang, G. (2023). Effect of strain on the electronic structure and optical properties of Cr-doped monolayer MoS_2. *Journal of Molecular Modeling*, *29*(11), 331. https://doi.org/10.1007/s00894-023-05735-w

[17] Saleem, S., Jameel, M. H., Yasin, A., Mayzan, M. Z. H. B., Ullah, A., Althubeiti, K., ..., & Bashir, J. (2024). A band gap and photoluminescence properties engineering in BaO semiconductor for ultraviolet (UV) photodetector applications: A comprehensive role of co-doping. *Journal of Colloid and Interface Science*, *670*, 599–616. https://doi.org/10.1016/j.jcis.2024.05.107

[18] Hajlaoui, R., Baachaoui, S., Ben Aoun, S., Ridene, S., & Raouafi, N. (2024). Surface tailoring of MoS_2 nanosheets with substituted aromatic diazonium salts for gas sensing: A DFT study. *ACS Omega*, *9*(36), 37953–37964. https://doi.org/10.1021/acsomega.4c04506

[19] Gong, C., Xiao, J., Zhu, L., Wang, Z., & Ma, S. (2019). Effect of deposition pressure on the microstructure and optical band gap of molybdenum disulfide films prepared by magnetron sputtering. *Coatings*, *9*(9), 570. https://doi.org/10.3390/coatings9090570

[20] Fano, U. (1961). Effects of configuration interaction on intensities and phase shifts. *Physical Review*, *124*(6), 1866–1878. https://doi.org/10.1103/PhysRev.124.1866

[21] Munkhbat, B., Wróbel, P., Antosiewicz, T. J., & Shegai, T. O. (2022). Optical constants of several multilayer transition metal dichalcogenides measured by spectroscopic ellipsometry in the 300–1700 nm range: High index, anisotropy, and hyperbolicity. *ACS Photonics*, *9*(7), 2398–2407. https://doi.org/10.1021/acsphotonics.2c00433

[22] Tang, Y., Zhang, Y., Ouyang, H., Zhao, M., Hao, H., Wei, K., ..., & Jiang, T. (2020). Ultrafast response of a hybrid device based on strongly coupled monolayer WS_2 and photonic crystals: The effect of photoinduced coulombic screening. *Laser & Photonics Reviews*, *14*(4), 1900419. https://doi.org/10.1002/lpor.201900419

[23] Li, X., Liang, J., Adair, K. R., Li, J., Li, W., Zhao, F., ..., & Sun, X. (2020). Origin of superionic $Li_3Y_{1-x}In_xCl_6$ halide solid electrolytes with high humidity tolerance. *Nano Letters*, *20*(6), 4384–4392. https://doi.org/10.1021/acs.nanolett.0c01156

[24] Qi, X., Lo, T. W., Liu, D., Feng, L., Chen, Y., Wu, Y., ..., & Ren, X. (2020). Effects of gap thickness and emitter location on the photoluminescence enhancement of monolayer MoS_2 in a plasmonic nanoparticle-film coupled system. *Nanophotonics*, *9*(7), 2097–2105. https://doi.org/10.1515/nanoph-2020-0178

[25] Sahoo, D., Tyagi, S., Agarwal, S., Shakya, J., Nasir, A., Yoo, W. J., & Kaviraj, B. (2023). Cost-effective and highly efficient manganese-doped MoS_2 nanosheets as visible-light-driven photocatalysts for wastewater treatment. *Langmuir*, *39*(20), 7109–7121. https://doi.org/10.1021/acs.langmuir.3c00390

[26] Zhang, R., Du, Y., Han, G., & Gao, X. (2019). Ferromagnetism and microwave absorption properties of Cr-doped MoS_2 nanosheets. *Journal of Materials Science*, *54*, 552–559. https://doi.org/10.1007/s10853-018-2841-z

[27] McMurdie, H. F., Morris, M. C., Evans, E. H., Paretzkin, B., Wong-Ng, W., Zhang, Y., & Hubbard, C. R. (1986). Standard X-ray diffraction powder patterns from the JCPDS research associateship. *Powder Diffraction*, *1*(4), 334–345. https://doi.org/10.1017/S0885715600012045

[28] Yee, K. (1966). Numerical solution of initial boundary value problems involving Maxwell's equations in isotropic media. *IEEE Transactions on Antennas and Propagation*, *14*(3), 302–307. https://doi.org/10.1109/TAP.1966.1138693

[29] Zaimia, R., Kaddour, S., Mastour, N., Baachaoui, S., Jemai, M., Ridene, S., & Raouafi, N. (2024). Effect of Ni-concentration on the linear and nonlinear optical properties of MoS_2 nanostructures. *International Journal of Modern Physics B*, *38*(24), 2450328. https://doi.org/10.1142/S0217979224503284

[30] Liu, C. H., Zheng, J., Chen, Y., Fryett, T., & Majumdar, A. (2019). Van der Waals materials integrated nanophotonic devices [Invited]. *Optical Materials Express*, *9*(2), 384–399. https://doi.org/10.1364/OME.9.000384

[31] Hu, F., Yi, H., & Zhou, Z. (2011). Wavelength demultiplexing structure based on arrayed plasmonic slot cavities. *Optics Letters*, *36*(8), 1500–1502. https://doi.org/10.1364/OL.36.001500

[32] Tumino, F., D'Agosta, P., Russo, V., Li Bassi, A., & Casari, C. S. (2023). Raman spectroscopy of 2D MoS_2 interacting with metals. *Crystals*, *13*(8), 1271. https://doi.org/10.3390/cryst13081271

[33] Wang, Y., Guo, Z., You, J., Zhang, Z., Zheng, X., & Cheng, X. (2019). Ultrafast nonlinear optical excitation behaviors of mono-and few-layer two dimensional MoS_2. *Photonic Sensors*, *9*, 1–10. https://doi.org/10.1007/s13320-018-0514-9

How to Cite: Kaddour, S., Zaimia, R., Mastour, N., Ridene, S., & Raouafi, N. (2025). Optical Transmission Enhancement of MoS_2 Nanosheets Doped with Magnetic Materials Ni, Mn, and Cr. *Journal of Optics and Photonics Research*. https://doi.org/10.47852/bonviewJOPR52023980